Wall collision and drug-carrier detachment in dry powder inhalers

Ariane, M.; Sommerfeld, M.; Alexiadis, A.

DOI:
10.1016/j.powtec.2018.04.051

Document Version
Publisher's PDF, also known as Version of record

Citation for published version (Harvard):
Ariane, M, Sommerfeld, M & Alexiadis, A 2018, 'Wall collision and drug-carrier detachment in dry powder inhalers: Using DEM to devise a sub-scale model for CFD calculations', *Powder Technology*, vol. 334, pp. 65-75. https://doi.org/10.1016/j.powtec.2018.04.051

Powder Technology 334 (2018) 65–75

Contents lists available at ScienceDirect

Powder Technology

journal homepage: www.elsevier.com/locate/powtec

Wall collision and drug-carrier detachment in dry powder inhalers: Using DEM to devise a sub-scale model for CFD calculations

M. Ariane [a,*], M. Sommerfeld [b], A. Alexiadis [c,*]

[a] Laboratoire Interdisciplinaire Carnot de Bourgogne, Université de Bourgogne Franche-Comté, Dijon, France
[b] Multiphase Flow Systems, Institute of Process Engineering, Otto-von-Guericke University Magdeburg, D-06230 Halle (Saale), Germany
[c] School of Chemical Engineering, University of Birmingham, Birmingham, United Kingdom

ARTICLE INFO

Article history:
Received 3 March 2018
Received in revised form 17 April 2018
Accepted 18 April 2018
Available online 25 April 2018

Keywords:
Discrete element method
Dry powder inhaler
Carrier with drug
Velocity
Rotation
Drug dispersion

ABSTRACT

In this work, the Discrete Element Method (DEM) is used to simulate the dispersion process of Active Pharmaceutical Ingredients (API) after a wall collision in dry powders inhaler used for lung delivery. Any fluid dynamic effects are neglected in this analysis at the moment. A three-dimensional model is implemented with one carrier particle (diameter 100 μm) and 882 drug particles (diameter 5 μm). The effect of the impact velocity (varied between 1 and 20 m s^{-1}), angle of impact (between 5° and 90°) and the carrier rotation (±100,000 rad s^{-1}) are investigated for both elastic and sticky walls. The dispersion process shows a preferential area of drug detachment located in the southern hemisphere of the carrier. The angle of impact with the highest dispersion is 90° for the velocities over 9 m s^{-1} and between 30° and 45° for lower velocities. The rotation of the carrier before the impact, on the other hand, for velocities higher than 7 m s^{-1}, plays a little role on the dispersion performance. The DEM results are finally "distilled" into a simplified analytic model that could be introduced as a sub-scale model in Euler/Lagrange CFD calculations linking fluid dynamics with the detachment probability of APIs in the inhaler.

1. Introduction

Dry powder inhalers (DPIs) are used for drug delivery to the respiratory tracts. The drug particles, the so-called Active Pharmaceutical Ingredient (API), need to be small enough (around 1 to 5 μm) in order to reach the deeper airways of the lungs. However, high cohesion inter-particle forces in these fine powders lead generally to the formation of agglomerates [1,2] which negatively affect the dispersion of APIs in the airflow [3]. To avoid this issue, larger particles (around 50 and 100 μm) called carrier particles are normally used; the surface of the carrier particle is coated with API particles and conveyed with the breathing flow through the inhaler. Under normal conditions, high turbulence and contact with the wall of the device ensure the detachment of the API particles and an effective delivery to the lungs [4]. Despite the abundance of DPIs in the worldwide market, however, the percentage of APIs that actually reach the lungs is only between 20 and 40%. Various techniques for increasing the efficiency of inhalation devices, therefore, have been proposed: (i) narrower inlet sections that increase air velocity and the probability of particle-wall impact [5] and (ii) grid insertion that concentrates turbulence in the inhaler swirl chamber [4,5]. In addition, the formulation of the powders can also play an important role in the penetration of the particles in the airway and the presence of high ratios of porous or elongated particles has been shown to be beneficial [4,6].

Other investigations have focused on the understanding of the mechanisms induced by flow and particle dynamics in inhaler chambers. Cui, et al. [7] and Sommerfeld and Schmalfuss [8] simulated the flow dynamics in a complete inhaler system and showed that the highest velocity and turbulent kinetic energy magnitudes are located in the swirl chamber. Milenkovic, et al. [9], Milenkovic, et al. [10] studied the particle flow dynamics in turbuhalers and focused on the location of the preferential particle deposition according to their sizes and the flow velocity. Tong, et al. [2] quantified the energy generated by the inter-particle collisions and particle-wall impacts and showed that the particle-wall collision energy is the predominant factor.

For ensuring an efficient drug delivery in the lungs, the API detachment from the carrier during the inhalation also needs to be maximised. Therefore, in recent years, micro-scale modelling of API-API and carrier-API interactions has gained interest. Cui, et al. [7] simulated one APIs-carrier agglomerate exposed to laminar plug or shear flow with different velocities and highlighted three mechanisms of detachment: lift-off, rolling and sliding. Cui and Sommerfeld [11] focused on the fluid dynamic forces acting on API particles with different properties such as their numbers (i.e. the degree of coverage APIs on carrier), API size and position. They showed that the normal and the tangential forces on the

* Corresponding authors at: School of Chemical Engineering, College of Engineering & Physical Sciences, University of Birmingham, B15 2TT, West Midlands, United Kingdom.
E-mail addresses: mostapha.ariane@u-bourgogne.fr (M. Ariane), a.alexiadis@bham.ac.uk (A. Alexiadis).

https://doi.org/10.1016/j.powtec.2018.04.051

APIs varied with the API position on the carrier and that the fluid dynamics forces acting on APIs are lower with smaller drug particles. More recently it was shown, that turbulence of the flow about the cluster carrier-APIs can remarkably enhance the detachment probability of APIs [12]. Sommerfeld and Schmalfuss [8] studied the fluid dynamics of inhaler devices (here a Cyclohaler) and the carrier particle motion in order to quantify the fluid stresses such as the velocity, the shear rate and the turbulent kinetic energy experienced by the carriers along their way through the inhaler. Their findings show the importance of the fluid forces, in particular, the transverse lift forces, on the particle velocity. Moreover, these studies revealed the extremely high wall collision rates experienced by the carriers.

Nevertheless, although all these studies give important information on fluid and particle motion in inhalers, APIs dispersion induced by wall impact remains limited to a few studies. [1,13] investigated the breakage of an APIs agglomerate (without carrier support) under different velocities, impact angles and agglomerate strengths. Using different geometries, these studies highlight the weak API-API cohesion after an impact and confirmed the key role of the wall impacts in term of impact energy. In the same way, with an API-carrier model, Tong, et al. [2,14], with an API-carrier model, investigated a number of parameters which play a role on the number of APIs detaching from the carrier after a wall impact. They showed, in particular, that the dispersion of APIs increases with the translational velocity and the angle of impact, and that the normal component of the impact velocity is the dominant factor. They also approximated the APIs dispersion performance with a cumulative distribution function of the impact energy and the adhesion energy. van Wachem, et al. [15], with a multi-scale approach, simulated the APIs dispersion with different adhesion forces. Their findings highlight the link between the properties of particles and the performance of the inhalers. They also demonstrate the relevance of using micro-scale results (APIs-carrier impact mechanisms) in a large macro-scale simulation (i.e. the inhaler device).

The aim of this work is to fill the gap between micro- and macro-scale simulations. Micro-scale models calculate the fraction of APIs detaching from the carrier given a certain impact energy, but do not relate this information to the actual hydrodynamic conditions occurring in the inhaler. Macro-scale simulations (e.g. CFD of inhalers), on the other hand, describe the hydrodynamics of the flow in the inhaler and, by means of Lagrangian particle-tracking, the trajectories of the carrier particles, but do not convert this information in a fraction of detaching APIs and, ultimately in the performance of the device. An attempt in this direction was undertaken by [16] who developed a wall collision-induced API detachment model to be used in the frame of Euler/Lagrange calculations. However, due to the high wall collision rates in inhalers, also the resulting API detachment rate was found to be very large.

In this work, the collision between a carrier-APIs agglomerate and a plane wall is modelled at the micro-scale by means of the Discrete Element Method (DEM) and the effect of impact velocity, angle of impact and angular velocity on the API detachment is investigated. The DEM results are then "distilled" into a simplified analytic model that can be introduced as a sub-scale model in Euler/Lagrange CFD calculations linking hydrodynamics with the detachment ratio or probability of APIs in the inhaler, or more in general, into multi-physics [17] simulations of the lungs airways [18].

2. Methodology

2.1. Modelling

The present study concerns the collision of carrier-API agglomerate with a plane wall which is simulated by DEM. Any fluid dynamic effects on particle motion are neglected at the moment. DEM is a Lagrangian particle tracking method where the particles are mostly treated as point masses with respect to possible fluid dynamic forces but it allows to handle multiple particle contacts and collisions (i.e. with surrounding other particles) generally in the frame of a soft-sphere collision model. Hence, here, by considering spherical particles (before and after impact), the particles move and rotate according to the Newtonian equations of motion [1].

$$m_i \frac{dv_i}{dt} = m_i \frac{d^2 r_i}{dt^2} = \sum_{i \neq j} \mathrm{F}_{i,j} + \sum \mathrm{F}_E, \tag{1}$$

$$I_i \frac{dw_i}{dt} = \sum_{i \neq j} \mathrm{R}_i \, \mathrm{F}_{i,j}, \tag{2}$$

where m_i is the mass of particle i, v_i its velocity, r_i its position, F_E the external forces, and $F_{i,j}$ the internal or inter-particle forces. I_i, w_i, and R_i, are respectively, the moment of inertia, the angular velocity and the radius of the particle i. External forces combine fluid dynamic forces acting on each individual particle (carrier and API) and external forces, such as gravity, which are however both neglected in this study.

In this work, the internal forces $F_{i,j}$ are the contact forces and account for (i) the non-adhesive elastic contact after a collision particle-particle or particle-wall based on the Hertzian theory and (ii) the adhesive contact between 2 spherical particles based on the Bradley model.

The Hertzian model consists of a normal contact force f^n and a tangential contact force f^t [19].

$$f^n = \sqrt{\delta}\sqrt{R_{eff}}\left(k_n \delta - m_{eff}\gamma_n v_n\right), \tag{3}$$

$$f^t = -\sqrt{\delta}\sqrt{R_{eff}}\left(k_t \xi + m_{eff}\gamma_t v_t\right), \tag{4}$$

where $R_{eff} = R_i R_j/(R_i + R_j)$, is the effective radius of the colliding particles i and j with radius R_i and R_j, k_n and k_t are the normal and tangential stiffness of the contact, δ and ξ the overlap and the displacement between the particles in, respectively, the normal and the tangential direction, γ_n and γ_t the normal and tangential damping coefficients and $m_{eff} = m_i m_j/(m_i + m_j)$ the effective mass of the colliding particles with mass m_i and m_j. The concepts of displacement ξ and, in particular, of overlap δ are abstract ideas that allow the DEM to calculate the tangential and normal forces occurring during collision. In reality, two colliding particles deform rather than overlap, but the idea is conceptually practical and it is going to be use also in the discussion section.

By considering elastic materials, k_n and k_t can be defined as [19,20].

$$k_n = \frac{2E_{i,j}}{3\left(1-\upsilon_{i,j}^2\right)}, \tag{5}$$

$$k_t = \frac{2E_{i,j}}{(2-\upsilon_{i,j})(1+\upsilon_{i,j})}, \tag{6}$$

with $E_{i,j}$ and $\upsilon_{i,j}$ are, respectively, Young's modulus and Poisson's ratio of particles i and j.

The adhesive contact between 2 spherical particles is modelled after Bradley [21].

$$\begin{cases} F_B(z) = F_c, & \text{for } z \le z_0 \\ F_B(z) = \dfrac{R_i R_j}{R_i + R_j}\dfrac{16\psi\pi}{3}\left[\dfrac{1}{4}\left(\dfrac{z}{z}\right)^{-8} - \left(\dfrac{z}{z}\right)^{-2}\right], & \text{for } z > z_0 \end{cases} \tag{7}$$

where F_B is the surface force between the particles i and j at a distance z, F_c is the maximum surface force when particles i and j are in contact ($z = z_0$), 2ψ the total surface energy of both surfaces per unit area and z_0 the equilibrium separation of the particles i and j. In our simulations, z_0 is equal to $4\ 10^{-10}$ m [22], ψ is deduced from Eq. (7) for $z = z_0$, and F_c is equal to $2.58\ 10^{-7}$ N (experimentally measured via Atomic Force Microscopy AFM) [7].

2.2. Geometry and model setup

A three-dimensional model is implemented and consists of one carrier particle with a diameter of 100 μm and 882 of mono-sized API particles with a diameter of 5 μm agglomerated around the carrier as a mono-layer (Fig. 1).

In API-carrier simulations, a degree of coverage is often used to define the number of APIs in contact with the carrier [7]. In the case of a mono-layer with mono-sized particles, the degree of coverage α is defined as the cross-section area of all API particles divided by the area of the sphere 'API + carrier' [7].

$$\alpha = \frac{n_{API}\frac{\pi}{4}d_{API}^2}{\pi(d_c + d_{API})^2}, \tag{8}$$

with n_{API} the number of API particles, d_{API} and d_c the diameter of one API particle and the carrier particle, respectively. Typical degrees of coverage are between 20% and 50% in pharmaceutical applications. In our simulations, we use a degree of coverage of 50% at $t = 0$ [7,16], which correspond to 882 API particles attached on the surface of the carrier.

The APIs and the carrier are considered elastic and their material properties are summarised in Table 1 [7]. Moreover, viscous dissipation can be easily implemented in DEM; but it is not considered here in order to compare our results with those of previous studies available in the literature [2,14]. The wall property effect is also investigated and, by modifying the damping coefficients (γ_n and γ_t in Eqs. (3) and (4)), different types of wall can be implemented (Table 1). Two walls are considered; an (1) "elastic" wall where both APIs and carrier have the same damping coefficients and can rebound after impacting the wall and a (2) "sticky" wall which only applies to the API. Consequently, those APIs which are detached from the carrier and then hit the wall will remain there and hence are deposited. Moreover, it should be reminded that an agglomerate-wall collision always happens with drug particle between carrier and wall, so that for the sticky wall condition the API will stick on the wall, but will detach from the carrier. This will have some effect on the deceleration of the agglomerate at shallow impact angles, as will be discusses in Section 3.3.

2.3. Simulation parameters

In this work, the influence of four variables on the agglomerate-wall collision is investigated: the translational and angular velocity v and w of the carrier-API, the axes of rotation, and the impact angle θ.

In our simulations, we vary the translational velocity from 1 m s^{-1} to 20 m s^{-1} (every 1 m s^{-1}) and we select 8 angles of impact between 5° to 90°. Moreover, three axes of rotation are chosen for the carrier: a rotation around the axis y (w_y in Fig. 1); a rotation around the axis perpendicular to the translational velocity $\vec{v}$ (w_{per} in Fig. 1); and a rotation around the axis parallel to the translational velocity $\vec{v}$ (w_{par} in Fig. 1). For these

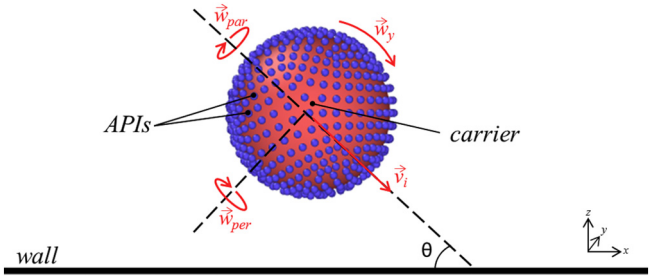

Fig. 1. Illustration of the carrier-API agglomerate approaching a plane wall with given translational and angular velocities at a pre-defined impact angle θ and definition of the coordinate system.

Table 1
Properties of carrier and APIs, contact parameters and model parameters used in the simulations (note the damping coefficients are specified for an elastic (1) and sticky (2) wall).

Model parameter	Value
Diameter of the carrier particle, d_c	100 μm
Diameter of one API particle, d_{API}	5 μm
Mass of the carrier particle, m_c	1.31 10^{-9} kg
Mass of the API particle, m_{API}	8.44 10^{-14} kg
Young's modulus of the carrier particle, E_c	63 GPa
Young's modulus of the API particle, E_{API}	2.15 GPa
Poisson's ratio of the carrier particle, ν_c	0.24
Poisson's ratio of the API particle, ν_{API}	0.3
Adhesion force	2.58 10^{-7} N (untreated glass carrier)
Normal damping coefficient of carrier γ_{nc}	(1) 0.3 (2) 0.3
Tangential damping coefficient of carrier γ_{tc}	(1) 0.15 (2) 0.15
Normal damping coefficient of API γ_{nAPI}	(1) 0.3 (2) 6 10^{14}
Tangential damping coefficient of API γ_{tAPI}	(1) 0.15 (2) 6 10^{20}

(1) "*elastic*" wall, (2) "*sticky*" wall.

three axes of rotation, a variation of the angular velocity magnitude of 2 10^5 rad s^{-1} is used between −1 10^5 rad s^{-1} and 1 10^5 rad s^{-1}.

The implementation of these series of variations including the "*elastic*" and the "*sticky*" wall condition brings it to a total number of 9600 simulations.

3. Results

In the following sections, the dispersion ratio η, defined as the number of detached APIs (after impact) over the initial total number of APIs, is calculated for each simulation. For literature comparison, we use here the same API and carrier material properties of [14]: the APIs and carrier are made of the same material with a density of 2650 kg m^{-3}, Young's modulus of 24 GPa, Poisson's ratio of 0.3 and an adhesion force of 2.99 10^{-9} N. The size ratio API/carrier is also 5/100, but the degree of coverage is lower, i.e. α = 15%, which means 242 APIs are distributed on the carrier.

A snapshot of a typical simulation is shown in Fig. 2. During the impact, the particles located in the southern hemisphere (i.e. facing the wall) tend to detach more easily than those located in the northern hemisphere. The reason of this behaviour, which also has been reported, but not explained, elsewhere [14], is discussed in Section 4.

3.1. Effect of translational velocity

The following simulations are based on the parameters of Cui, et al. [7] as provided in Table 1. Thereby it is possible to consider also realistic impact velocities as observed in an inhaler [8]. The effect of the impact angle and translational velocity on the dispersion ratio is shown in Fig. 3. In these simulations, the angular velocity is set to zero. As expected, higher velocities yield to higher dispersion ratios over the entire angular range due to the higher inertial forces at impact. The trend in the dispersion ratio curves is very similar for all absolute values of the impact velocity and, at shallow angles, low values are observed (only at 1 m s^{-1} and 5°, the dispersion ratio is equal to zero) which continuously increase with impact angle and reach a maximum. For velocities above 9 m s^{-1}, the dispersion ratio is maximal at 90° [14] with a neglected effect of the impact angle, while for lower velocities is located between 30° and 45°. This behaviour has also been observed, but not explained, by [2]. More details on this are given in Section 4.

3.2. Effect of rotational velocity

In this section, the effect of the agglomerate (carrier-API) initial rotation is investigated. In order to highlight the specific effect of each axis of rotation, we implement separately the angular velocities w_y,

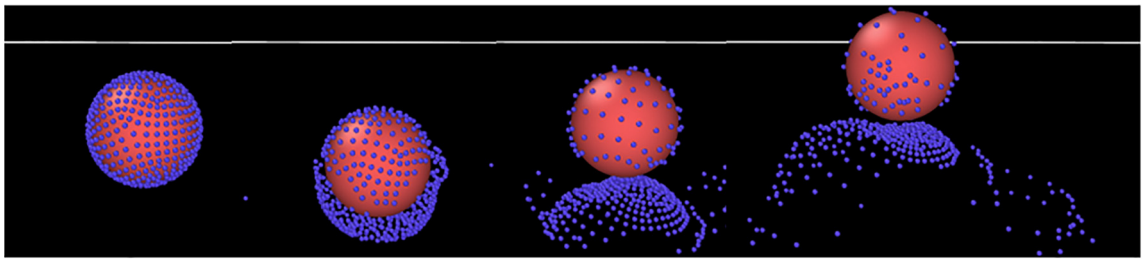

Fig. 2. Snapshots of the impact carrier-API agglomerate with the wall at different times for $v = 0.1$ m s^{-1}, $\theta = 45°$, $F_c = 2.99\ 10^{-9}$ N and $\alpha = 15\%$.

w_{par} and w_{per} as explained in Section 2.3. The DEM results show that, above $v = 7$ m s^{-1}, the dispersion is not significantly affected by the angular velocity (in any direction). Below 7 m s^{-1}, differences are only observed for angular velocities in the y-direction, i.e. axis of rotation perpendicular to the wall collision plane. Fig. 4 shows how the initial angular velocity of the carrier affects the dispersion at $v = 5$ m s^{-1}. The fact that only w_y affects the dispersion depends on the fact that, given our coordinate system (Fig. 1), during the collision the tangential forces transfer part of the linear momentum in the x-direction into angular momentum in the y-direction. This does not occur with w_{par} and w_{per} that remain approximately constant during the collision. Therefore, positive w_y causes an actual acceleration of the carrier after rebound and negative w_y yields a deceleration; both affecting the detachment. Fig. 5 provides an example of how v_x and w_y are linked. If w_y is positive (Fig. 5a), v_x increases during the impact. If w_y is negative, v_x decreases during the impact and, in the case of (Fig. 5b), the carrier even bounces backwards after the collision (a similar effect is known as "sidespin" in cue sports). This circumstance plays a role in the detachment, but it is not always easy to anticipate its effect on the detachment without the actual DEM simulation as discussed in Section 4. The detachment rate for positive w_y (Fig. 5a) is remarkably below the result without rotation until an impact angle of 60°, but then becomes higher (Fig. 4). For negative w_y, the trends are not that clear. At high impact angle (beyond 60°) again the detachment ratio is larger than without rotation and almost identical to the result with positive rotation. At smaller impact angles negative rotation is only effective for an impact angle of 20° giving a remarkable reduction. For the other two directions of rotation (i.e. w_{par} and w_{per}) the dispersion ratio is recognisable increased for impact angles beyond 60°, otherwise it is almost identical to the result without rotation. In conclusion, agglomerate (carrier-API) rotation has important effects on the API detachment for low translational impact velocities. For higher impact velocities the agglomerate surface velocity is not that much influenced when having angular velocities in the considered magnitude. In wall-bounded flows, such as an inhaler device, these high rotational velocities are definitely realistic and mainly induced by previous agglomerate or carrier wall collisions (see for example [23]). Assuming a sticking wall collision (all translational energy is transformed to rotational energy) of the agglomerate (effective diameter 110 μm) with a wall-parallel velocity of 10 m s^{-1}, the angular velocity will be 200,000 rad s^{-1}.

3.3. Effect of wall properties

The rebound of the API-carrier agglomerate after impact with two different walls is shown in Fig. 6. The detachment process is similar in both cases with a preferential detachment located in the southern hemisphere. A difference is observed on the motion of the detached APIs after impact. In the case of "*elastic*" wall (Fig. 6a), detached APIs maintain a certain velocity and rebound with the carrier. In the case of "*sticky*" wall (Fig. 6b), after detachment, the APIs remain attached on the wall (Fig. 6b), which means, they are deposited and hence need to be re-entrained into the flow inside an inhaler device by fluid dynamic forces (see for example [11]). Since for such small particles the wall adhesion is very strong, deposited APIs would most probably not leave the inhaler and thereby yield low fine particle release efficiency.

Similarly, Fig. 7 indicates that the detachment ratio is not particularly affected by the nature of the wall and the only significant difference occurs at $v = 19$ m s^{-1} and for angles below 20°.

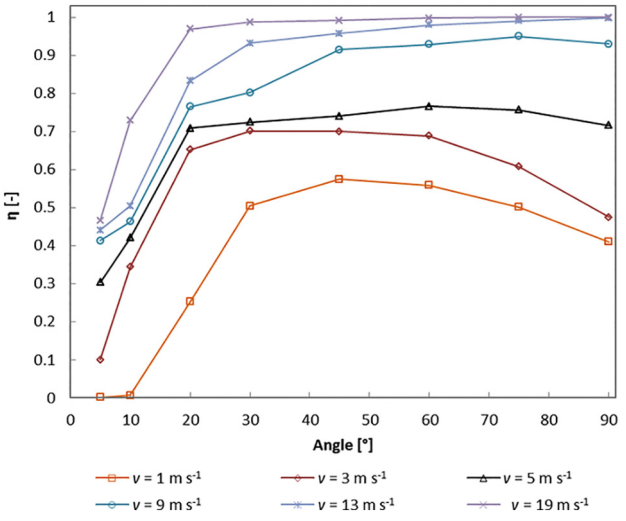

Fig. 3. Effects of the impact angle and the translational velocity on the dispersion ratio for the case of "*elastic*" wall and $w = 0$ (other parameters according to Table 1).

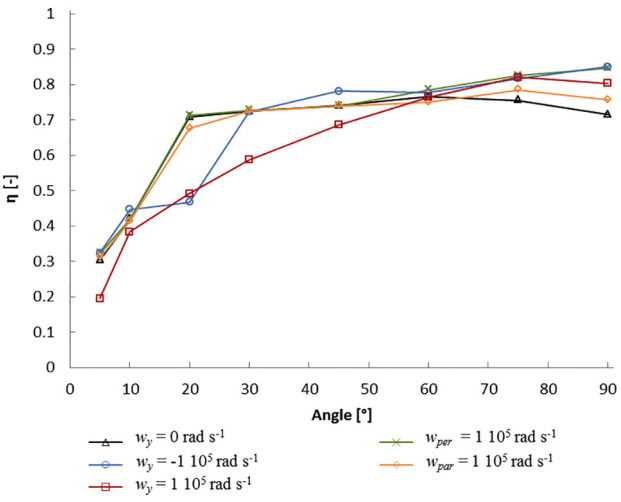

Fig. 4. Effects of the impact angle and the angular velocity magnitude on the dispersion ratio for the case of "*elastic*" wall and $v = 5$ m s^{-1} (other parameters according to Table 1).

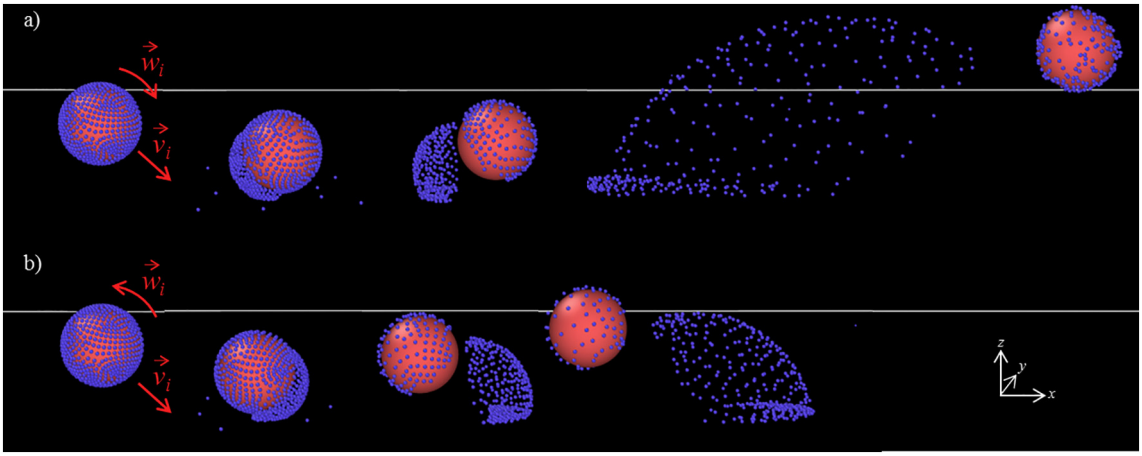

Fig. 5. Snapshots of the impact API-carrier on "*elastic*" wall at different times for $v = 1$ m s^{-1}, $\theta = 45°$ and an initial rotation in the y-direction (a) $w = 1\ 10^5$ rad s^{-1} and (b) $w = -1\ 10^5$ rad s^{-1} (other parameters according to Table 1).

When the carrier moves with very small angles close to the wall, even if the impact energy is not enough to detach the APIs, the "*sticky*" wall can capture the small particles trapped between the carrier and the wall like a sort of flypaper. This occurs, in particular, at higher velocities when the overlap δ is larger and, therefore, there are more APIs caught in between the carrier and the wall.

Consequently a correct prediction or modelling of the deposited fraction of APIs is essential to forecast the fine particle fraction leaving the inhaler. Therefore, also in an Euler/Lagrange prediction of the efficiency of inhaler devices, the deposition of the API needs to be modelled realistically.

Finally, most of the time, the wall is neither fully elastic nor completely sticky. In this study, we decided to simulate the two extreme cases and examine the differences. Fig. 7, for instance, shows that the stickiness of the wall plays a role only at high velocities and low angles.

4. Discussion

4.1. Wall collision model

For a detailed analysis and optimisation of inhaler devices the classical Euler/Lagrange approach is most suitable due to its efficiency (for further references see [7,8]). However, in this approach, the tracked particles, the carriers or agglomerates, are considered as point masses. Consequently all phenomena occurring on the scale of the particles, such as drug particle detachment from the carrier have to be modelled appropriately. Such detachment may occur by fluid dynamic forces or due to wall impacts. The probability of fluid dynamic detachment is quite low [11], so that the dominant mechanism of drug particle redispersion from a carrier is wall impact, which frequency is extremely high [8]. For considering such an inertial drug detachment in the

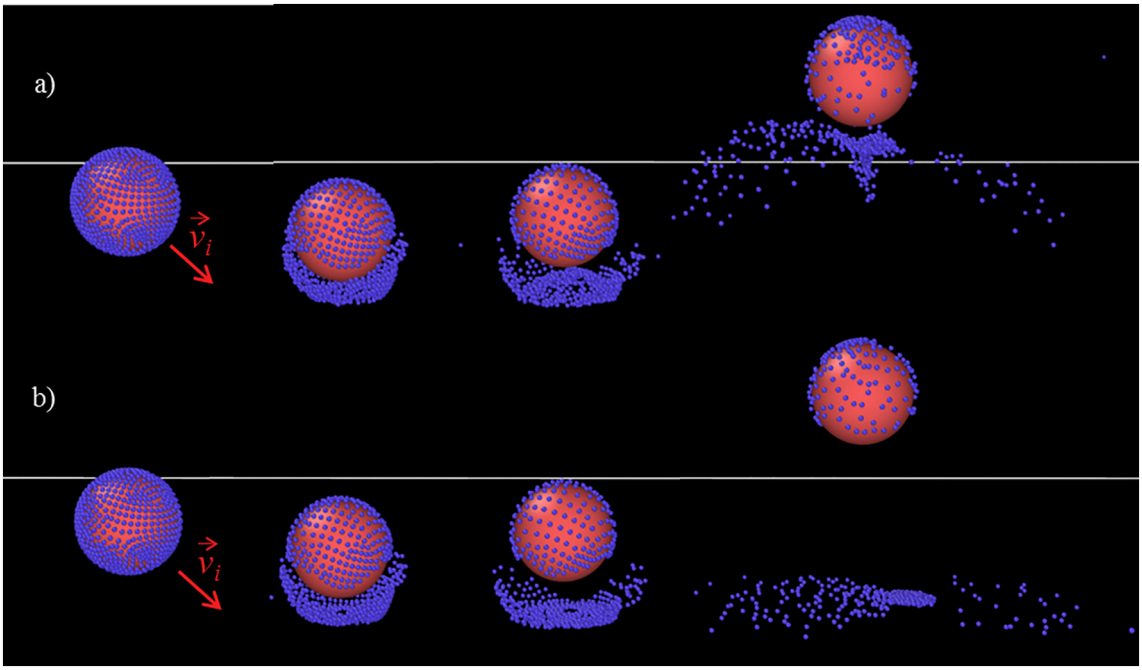

Fig. 6. Snapshots of the impact API-carrier at different times for $v = 1$ m s^{-1}, $\theta = 45°$ for (a) "*elastic*" wall (a) versus "*sticky*" wall (b) (other parameters according to Table 1).

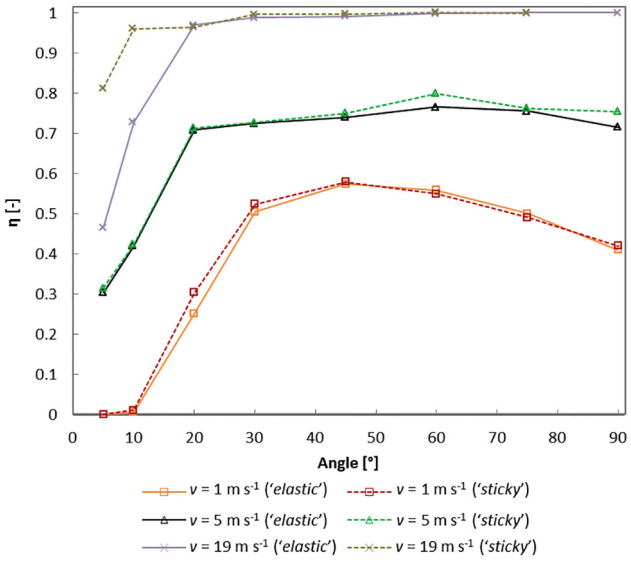

Fig. 7. Effects of the impact angle and the translational velocity on the dispersion ratio in the case of "*elastic*" wall and "*sticky*" wall (other parameters according to Table 1).

frame of Euler/Lagrange calculations, Cui and Sommerfeld [16] developed a carrier-wall collision model with API detachment. This model is however rather sophisticated and associated with a number of strongly simplifying assumptions. Moreover, due to the high number of wall collisions, the drug detachment probability was found to be close to 100%. With the conducted DEM simulations, now it is possible to deduce a much simpler wall collision model which also can be validated based on the produced data.

4.1.1. Collision between carrier and wall

Initially, we look at the collision of the carrier with the wall and we can simplify the collision process in three main steps (Fig. 8). When the particle hits the wall, its angular velocity is w and its translational velocity is v with its perpendicular and parallel (to the wall) components respectively.

$$v_{\perp} = v \sin\theta, \tag{9}$$

$$v_{//} = v \cos\theta, \tag{10}$$

During the collision, the DEM simulation calculates the overlap δ_w and the displacement ξ_w between the wall and the carrier. The overlap and the displacement do not actually occur in a real collision, but, as mentioned, are abstract concepts used by the DEM solver to calculate the contact normal and tangential forces f^n and f^t (Eqs. (3) and (4)).

The collision is fully elastic and there is no dissipation (if necessary, dissipation could be introduced in the form of a restitution coefficient). However, the value of v changes before and after the collision. Due to f^t, in fact, part of the tangential kinetic energy is transformed in rotational kinetic energy. The parallel velocity $v_{//}$ does not remain constant (becomes $v'_{//}$) and part of the linear kinetic energy lost (or gained) goes into the angular velocity w (that becomes w'). In theory, if the collision is elastic, this should affect only the parallel velocity. The situation, however, is considerably complicated by the presence of a layer of APIs between the carrier and the wall and, usually, there is also a (smaller) change of perpendicular velocity $v_{\perp}$ that becomes $v'_{\perp}$.

4.1.2. API's escape velocity

Initially, the APIs move with the carrier. At equilibrium, the overlap δ between the carrier and the API can be calculated from the balance of forces.

$$f^n\delta - F_B\delta = 0. \tag{11}$$

In the case of Hertzian contact, Eq. (11) gives.

$$\delta = \left(\frac{F_B}{\sqrt{R_{eff}}k_n}\right)^{\frac{2}{3}}. \tag{12}$$

After the carrier hits the wall, the relative velocity between the two particles suddenly changes. We can distinguish two cases (Fig. 9). If the relative velocity of the API is above a certain critical velocity (i.e. the escape velocity v_e), the kinetic energy overcomes the work done by the adhesion force and the particle detaches from the carrier-wall collision, it returns to its initial value while the relative velocity ($\Delta v = v_{API} - v_{carrier}$) returns to zero (Fig. 9). Only particles whose relative velocity is higher than v_e detach from the particle. In principle, there is not a simple way to determine the relative velocity without the DEM simulation. In the following sections, however, we discuss two typical detachment scenarios (or modes) and, based on these, a simplified model, which can estimate the dispersion ratio without the need of carrying out a DEM simulation, is proposed.

4.2. Detachment modes

Initially, we neglect the angular velocity. This means that no energy is transferred from the linear to the rotational velocity and, since the collision is elastic, $v = v'$, $v_{//} = v'_{//}$, and $v_{\perp} = v'_{\perp}$ in Fig. 8. The carrier and the APIs, therefore, have, at all times, the same parallel velocity $v_{//}$ and the detachment only depends on the perpendicular velocity. In this case, the dynamics differs if the API is located at the northern or the southern

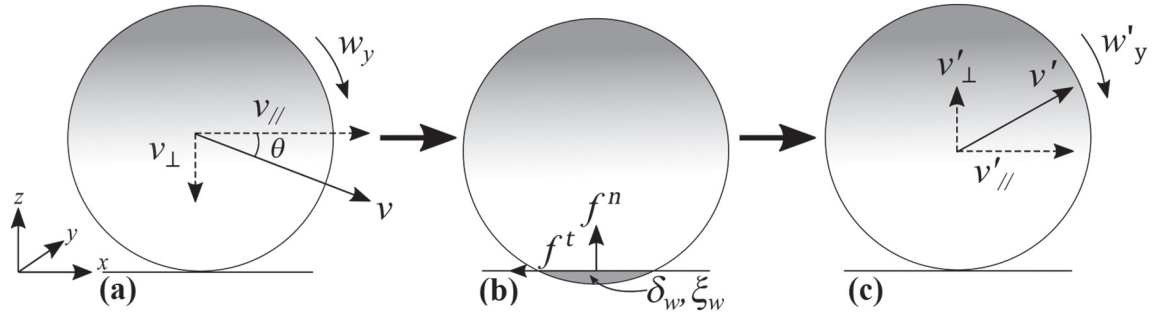

Fig. 8. Schematic representation of the carrier collision: (a) impact, (b) overlap and (c) rebound.

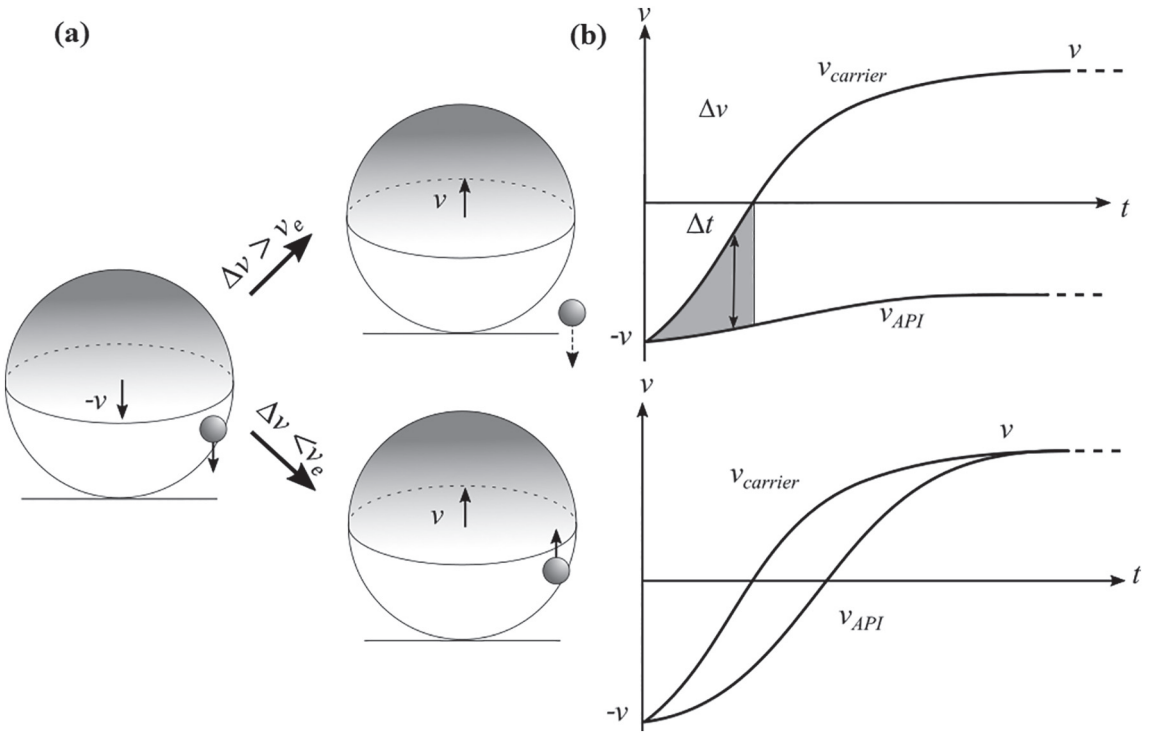

Fig. 9. Relative velocity between API and carrier and escape velocity v_e; (a) the two types of carrier-wall collision scenarios, $\Delta v > v_e$ escape, $\Delta v < v_e$ remain; (b) change of carrier and API velocities during wall collision for escape and remain of API.

hemisphere of the carrier. We propose two simplified models of detachment one for the northern hemisphere and another for the southern hemisphere.

4.2.1. Southern hemisphere detachment

The collision with the wall reduces abruptly the perpendicular component of the carrier velocity. As a consequence, the relative velocity of an API located on the southern hemisphere increases as shown in Fig. 10. As mentioned, since the collision is elastic and, for the moment, we neglect the angular velocity, the parallel velocity of both particles is not affected by the collision and, therefore, the relative velocity Δv has only a perpendicular component (Fig. 10).

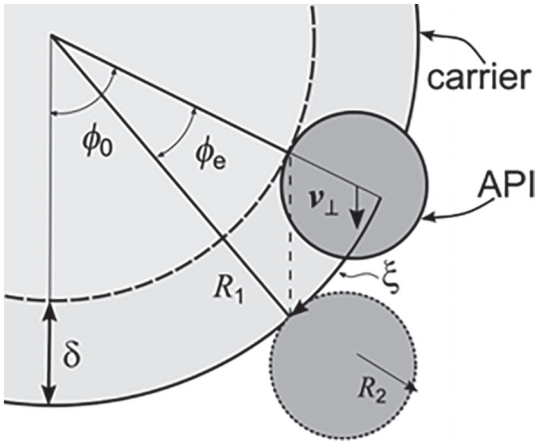

Fig. 10. The Southern hemisphere detachment (overlap oversized for explanation purposes).

The kinetic energy of the API is.

$$E_K(t) = \frac{1}{2} m[\Delta v_\perp(t)]^2. \tag{13}$$

The relative velocity $\Delta v_\perp$, however, changes with time. Eq. (13) can be simplified by considering an average relative velocity $<\Delta v_\perp>$ during the detachment process. The DEM simulations show that the detachment occurs during the first part of the collision (Δt in Fig. 9, the time required for the carrier to stop before the rebound). As a first approximation, we can use $<\Delta v_\perp> = \frac{1}{2} v_\perp$ (averaging over the "almost triangular" grey area in Fig. 9) and, accounting for Eq. (9), an estimate of the kinetic energy of the API during detachment, therefore, is.

$$E_K \approx \frac{1}{8} m v^2 \sin^2\theta. \tag{14}$$

During the detachment, the work done by the adhesion force can be calculated as.

$$E_B = \int_{-\delta}^{\infty} F_B(z) dz, \tag{15}$$

where F_B is given by Eq. (7). An estimate of E_B, which does not require the calculation of the integral is.

$$E_B \approx F_C\left(z_0 + \delta + \frac{z_{cut-off}}{2}\right), \tag{16}$$

where $z_{cut\text{-}off}$ is a cut-off distance, after which adhesion force is negligible and is calculated to approximate Eq. (16) with Eq. (15); here $z_{cut\text{-}off} = 10^{-9}$ m.

The work done by f^n can be calculated by.

$$E_n = \sqrt{R_{eff}}k_n \int_0^{\delta} z^{\frac{3}{2}}dz = \frac{2}{5}\sqrt{R_{eff}}k_n\delta^{\frac{5}{2}}, \tag{17}$$

where the displacement δ is calculated from Eq. (12).

The tangential force acting on the particle is $\min(f^t, \mu f^n)$, where μ is the static friction coefficient and f^t is given by Eq. (4). To simplify our calculations, we estimate the work done by the tangential force only on the basis of μf^n since, only when the tangential force reaches this value, the API begins to move relatively to the carrier.

$$E_t \approx \mu\sqrt{R_{eff}}k_n\delta^{\frac{3}{2}}\xi. \tag{18}$$

The tangential displacement can be estimated as Fig. 10.

$$\xi \approx R_1\phi_e, \tag{19}$$

where R_1 is the radius of the carrier and ϕ_e the escape angle (Fig. 10). Geometric considerations bring to.

$$(R_1-\delta)\ \sin\phi_0 = R_1\ \sin(\phi_0-\phi_e), \tag{20}$$

and

$$\phi_e = \phi_0 - \sin^{-1}\left(\frac{R_1-\delta}{R_1}\ \sin\phi_0\right), \tag{21}$$

where ϕ_0 is the angle of the initial position of the API on the carrier surface. Since $R_1 \gg \delta$, Eq. (21) can be expanded in Taylor series as.

$$\phi_e = \frac{\delta}{R_1}\ \tan\phi_0 + O\left(\delta^2\right), \tag{22}$$

and Eq. (18) becomes.

$$E_t \approx \mu\sqrt{R_{eff}}k_n\delta^{\frac{5}{2}}\ \tan\phi_0. \tag{23}$$

From Fig. 10, we see that the elastic force tends to detach the two particles, while the tangential force opposes sliding. By writing the energy balance of the API, therefore, we can determine that detachment is only possible if the kinetic energy and the elastic energy overcome the adhesion and tangential energies i.e.

$$E_k \geq E_B - E_n + E_t. \tag{24}$$

The symbol "≥" becomes "=" when the API's velocity is exactly the escape velocity (i.e. $v = v_e$). By combining together Eqs. (15), (16), (23) and (24), we can estimate the escape velocity as.

$$v_e \approx \sqrt{\frac{F_c(\delta + z_{cut-off}) - \frac{2}{5}\sqrt{R_{eff}}k_n\delta^{\frac{5}{2}} + \mu\sqrt{R_{eff}}k_n\delta^{\frac{5}{2}}\ \tan\phi_0}{\frac{1}{8}m\ \sin^2\theta}}, \tag{25}$$

Eq. (25) tells us that if the initial velocity of the API particle is higher than v_e, the particle detaches otherwise it remains on the carrier. However, the detachment velocity is not everywhere the same. Since Eq. (25) depends on $\tan\phi_0$, v_e is minimal at the south pole and maximal at the equator of the carrier. By rearranging Eq. (24), we can determine the critical angle $\phi_{0,}$ below which, given an initial velocity v, detachment occurs.

$$\phi_0 \approx \tan^{-1}\left(\frac{\frac{1}{8}mv^2\ \sin^2\theta - F_c(\delta + z_{cut-off}) + \frac{2}{5}\sqrt{R_{eff}}k_n\delta^{\frac{5}{2}}}{\mu\sqrt{R_{eff}}k_n\delta^{\frac{5}{2}}}\right), \tag{26}$$

Assuming the initial particle API distribution is uniform on the carrier surface (Fig. 11), from ϕ_0, we can calculate the dispersion ratio as.

$$\eta_{SOUTH} = \frac{\text{Detachment Area}}{\text{Total Area}} = \begin{cases} \frac{1-\cos\phi_0}{2} & \text{if } \phi_0 > 0 \\ 0 & \text{if } \phi_0 \leq 0 \end{cases} \tag{27}$$

The maximum dispersion ratio occurs when $\phi_0 = \pi/2$ and the APIs on whole southern hemisphere detach.

4.2.2. Northern hemisphere detachment

The same logic, however, does not apply to the northern hemisphere (Fig. 12).

In this case, the API cannot move in the perpendicular direction, but only in the direction tangential to the carrier surface. This means that the relative velocity is $\Delta v = v_\perp \cos\varphi_0 = v\cos\varphi_{0,}\sin\theta$. The displacement ξ, on the other hand, can be calculated by.

$$\xi = \sqrt{R_1^2 - (R_1-\delta)^2} \approx \sqrt{2R_1\delta}. \tag{28}$$

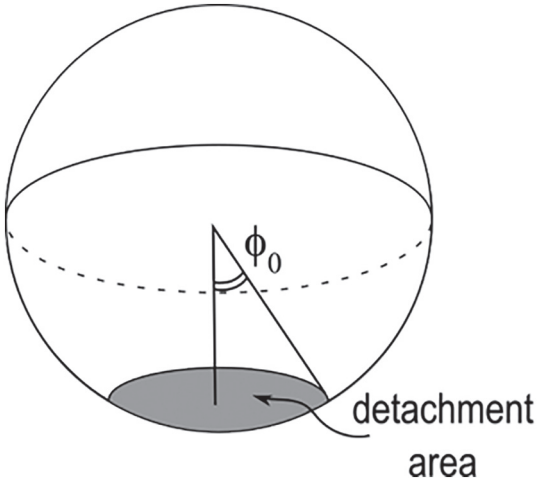

Fig. 11. Illustration of the detachment area on the southern hemisphere of the carrier particle.

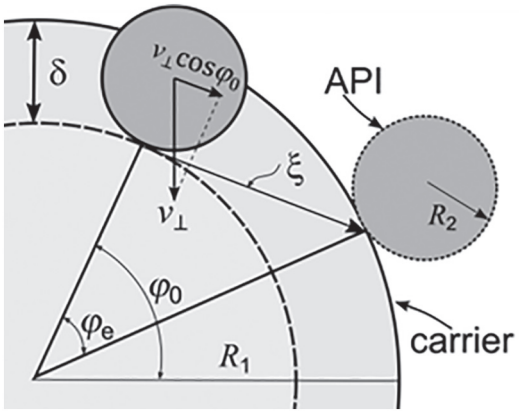

Fig. 12. Illustration of the detachment of API from the northern hemisphere of the carrier.

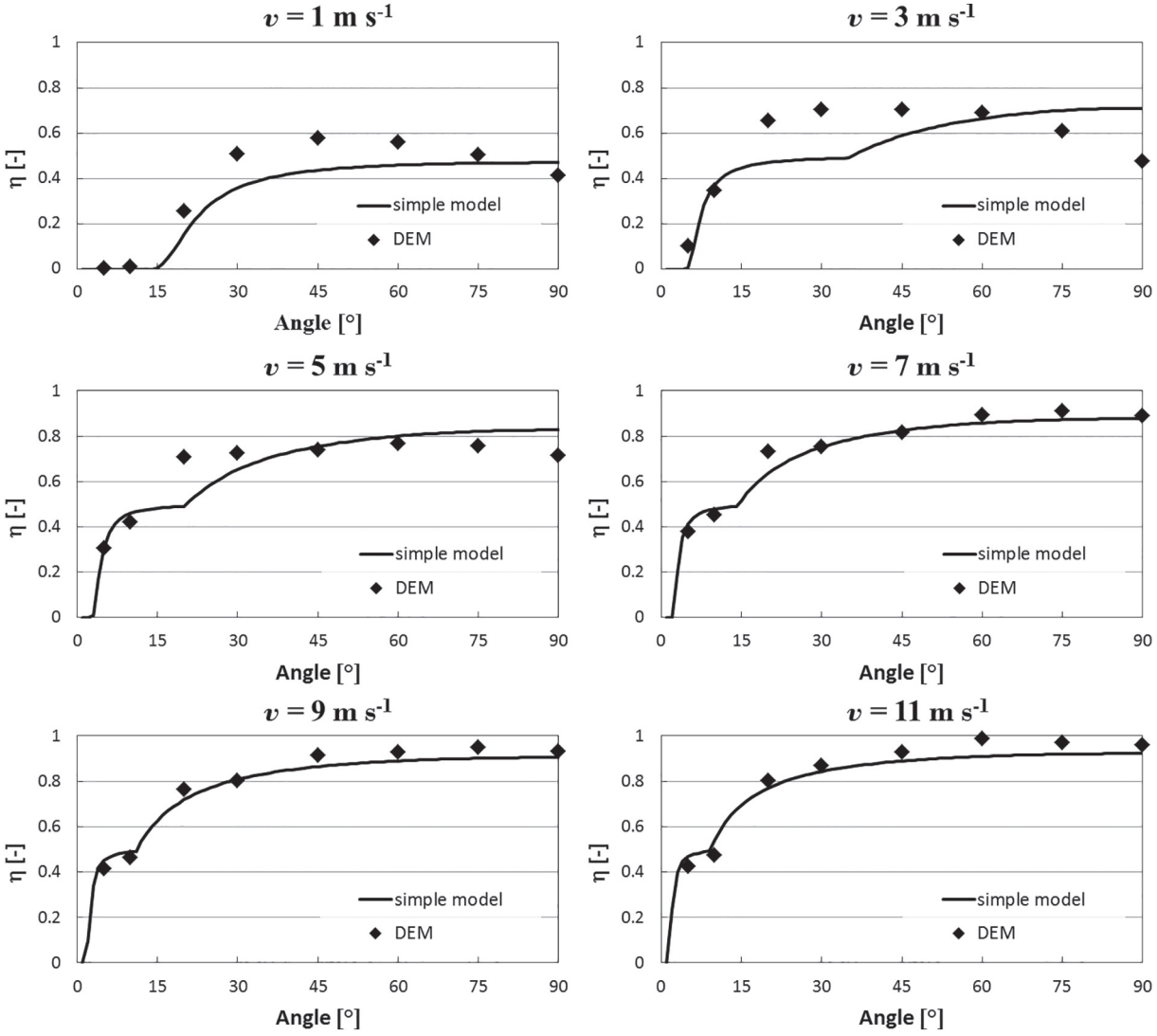

Fig. 13. Dispersion ratio as a function of impact angle, comparison between the simple analytic model and the DEM results for different magnitudes of the carrier impact velocity.

The energy balance, in this case, is obtained by:

$$\frac{1}{2}mv^2\cos^2\varphi_0\sin^2\theta = F_c(\delta + z_{cut-off}) - \frac{2}{5}\sqrt{R_{eff}}k_n\delta^{\frac{5}{2}} + \mu\sqrt{R_{eff}}k_n\delta^{\frac{3}{2}}\sqrt{2R_1\delta}. \quad (29)$$

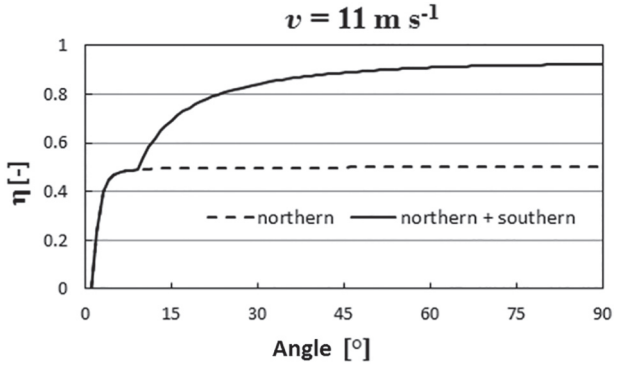

Fig. 14. η_{NORTH} and η_{SOUTH} components of the total dispersion ratio η.

The critical angle φ_0 below, which detachment occurs, now satisfies the relation.

$$\cos\varphi_0 = \sqrt{\frac{F_c(\delta + z_{cut-off}) - \frac{2}{5}\sqrt{R_{eff}}k_n\delta^{\frac{5}{2}} + \mu\sqrt{R_{eff}}k_n\delta^{\frac{3}{2}}\sqrt{2R_1\delta}}{\frac{1}{2}mv^2\sin^2\theta}}. \quad (30)$$

From $\cos\varphi_0$, we can calculate the dispersion ratio in the northern hemisphere as.

$$\eta_{NORTH} = \frac{1-\cos\varphi_0}{2}. \quad (31)$$

Finally, the overall dispersion ratio can be calculated by.

$$\eta = \eta_{NORTH} + \eta_{SOUTH} \quad (32)$$

The simple model in Eq. (32) is based on several simplifications and approximations and gives a crude estimate of the actual dispersion ratio. Fig. 13 shows the comparison between DEM results and the developed simple model. The simple model is more accurate for velocities higher than 7 m s^{-1}. The "composite" look of some of the profiles generated by the simple model in Fig. 13 depends on the fact that Eq. (32) is the result of the two components η_{NORTH} and η_{SOUTH}.

Fig. 14 exemplifies this point. The maximum possible value of both η_{NORTH} and η_{SOUTH} is 0.5 since each of them only refers to a hemisphere. The final dispersion ratio η is the sum of η_{NORTH} and η_{SOUTH}.

4.3. Rotating particle

The simplified model derived in the previous section does not account for the rotation of the carrier. This is not a problem for higher impact velocities, since above $v = 7$ m s^{-1}, the DEM results show that the initial angular rotation does not significantly affect the results. At lower velocities, however, the effect of the angular velocity, and in particular w_y, can be perceived even if initially $w_y = 0$. This happens because the carrier starts rotating during the collision as an effect of the tangential force f^t. The maxima (Fig. 13) at $v = 1$ m s^{-1} and $v = 3$ m s^{-1}, for instance, depend on the change of parallel velocity $v_{//} \rightarrow v'_{//}$ (Fig. 8), which, in turn, depends on the change of angular velocity from $w_y \rightarrow w'_y$ as explained in Section 4.1.1.

Fig. 15 shows, for $v = 5$ m s^{-1} and different initial angular velocities, the absolute value of the variation of v_x during the collision. Since in this case v_x changes, the API particles (besides accelerating in the z-direction as explained in Sections 4.2.1 and 4.2.2) also accelerate in the x-direction. The magnitude of the acceleration can be expressed as.

$$a_x = \frac{|\Delta v_x|}{\Delta t}. \tag{33}$$

where Δt is the duration of the collision. Δt changes for each θ, but if we compare $|\Delta v_x|$ at the same θ, we can notice a correspondence between Figs. 15 and 4: the case among $w_y = 0$, $w_y = 10^5$ rad s^{-1} and $w_y = -10^5$ rad s^{-1}, that has the highest $|\Delta v_x|$ has also the highest dispersion and, vice versa, the case that has the lowest $|\Delta v_x|$ has also the lowest dispersion.

The only exception is $\theta = 20°$ that seems to behave differently both in terms of dispersion and $|\Delta v_x|$. Looking at the DEM simulation and data, we could not understand the reasons that make this specific case different from the others.

Although, Fig. 15 explains the observed differences in the DEM results between the cases of $w_y = 10^5$ rad s^{-1} and $w_y = -10^5$ rad s^{-1}, it doesn't clarify why the simplified model is also valid with particle rotation for high velocities. In fact, the explanation is given with the help of Fig. 16.

At the beginning, the carrier has a certain amount of linear kinetic energy and a certain amount of rotational kinetic energy based on its initial linear (v_0) and angular (w_0) velocity. During the collision, the change of linear kinetic energy is.

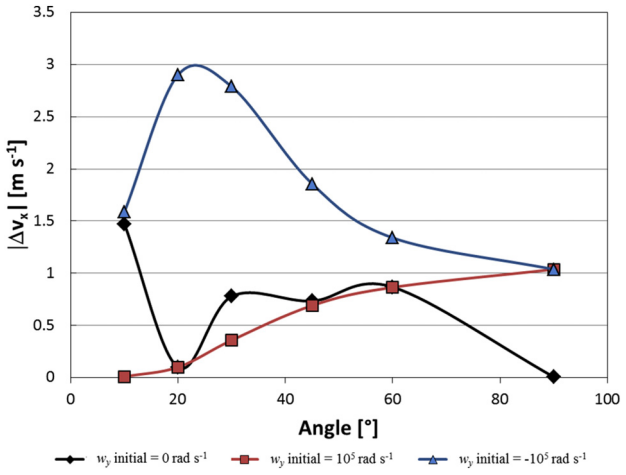

Fig. 15. Absolute value of the change of v_x during collision for different initial angular velocities ($v = 5$ m s^{-1}).

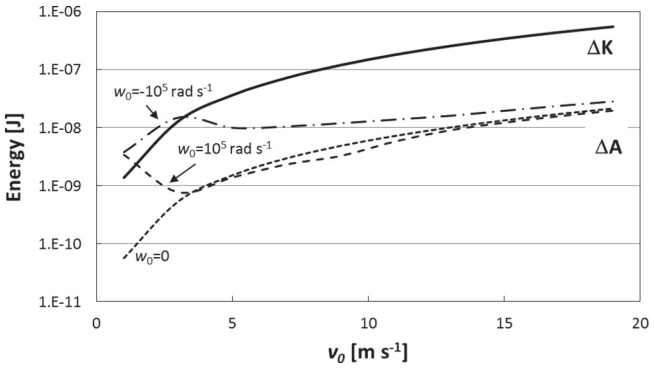

Fig. 16. Energy change for linear kinetic energy (ΔK) and rotational energy (ΔA) at different initial velocities (v_0) and angular velocities (w_0) for a 45° angle.

$$\Delta K = \frac{1}{2} m (v - v_0)^2, \tag{34}$$

where v is the velocity after the impact. The change of rotational energy is.

$$\Delta A = \frac{1}{2} I (w - w_0)^2, \tag{35}$$

where w is the angular velocity after the impact. Fig. 16 shows ΔK and ΔA for different initial velocities (v_0 between 1 and 19 m s^{-1}) and angular velocities ($w_0 = -10^5$, 0 and 10^5 rad s^{-1}) for a 45° collision (other angles show qualitatively similar profiles). The change of linear energy is almost the same for all three w_0 considered and, therefore, only ΔK for $w_0 = 0$ is reported in Fig. 16.

Fig. 16 shows that, as the impact velocity v_0 increases, both ΔK and ΔA increase. However, for v_0 above 7 m s^{-1}, ΔK is at least one order of magnitude higher than any ΔA curve in Fig. 16. This explains why, for $v_0 > 7$ m s^{-1}, the initial angular velocity does not significantly affect the dispersion ratio: the change of momentum, which generates the APIs' detachment, is mostly due to the change of linear velocity rather than the angular velocity. The same reason is behind the fact that, despite the simplified model does not account for angular velocity, for $v_0 > 7$ m s^{-1} it works well even for the case of rotating particles.

5. Conclusions

In this study, we used the DEM to simulate the collision of a drug-carrier with the walls of a dry powder inhaler device and the consequent detachment of the APIs. The objective is to evaluate the influence of the impact velocity, angle and angular velocity of the carrier on the dispersion ratio which is the number of drug particles detached to that initially placed on the carrier. The main conclusions fore the case without agglomerate (carrier and APIs) rotation are:

- With increasing impact angle the dispersion ratios increase rapidly towards a maximum value.
- High dispersion ratios are already reached above impact angles of 20°; except for very low velocities (i.e. 1 m s^{-1}) which are rarely found in inhalers [8].
- Expectedly, increasing impact velocity yields higher dispersion ratio; at low velocity (~1 m s^{-1}) the maximum is around 50%, whereas at high velocity (~20 m s^{-1}) the dispersion ratio is close to 100% already for a wide range of impact angles (i.e. between 20° and 90°).

Agglomerate or carrier particle rotation in inhaler devices mainly occurs due to wall collisions and depending on the type of collision and

the impact velocity can reach extremely high values. From the present study it may be concluded:

- Agglomerate rotation is of importance if the agglomerate kinetic energy resulting from rotation is below that of the translational velocity.
- For these cases rotation reduces the dispersion ratio by up to 20% for impact angles below 60° and slightly increases API detachment for larger impact angles.

An "*elastic*" or "*sticky*" wall for the API particles has only marginal effects on the API dispersion ratio for all impact velocities considered. Only at a high impact velocity (i.e. 20 m s^{-1}) the dispersion of API is improved at impact angles below 20°. However, due to the wall stickiness, the API will be remaining (i.e. deposition) on the wall although detached from the carrier. Therefore, effectively these drug particles are also not re-dispersed into a flow and will probably remain in the inhaler reducing its efficiency. In future studies also this deposition needs to be investigated in more detail and also modelled more realistically for an Euler/Lagrange calculation.

Based on the DEM data, we propose a simplified analytic model, which provides a good approximation of the DEM results at high impact velocities (in this case $v > 7$ m s^{-1}). The simplified model does not account for the change of angular velocity during the impact, and the data show that, above 7 m s^{-1}, the angular velocity does not particularly affect the dispersion.

The aim of the simplified model is twofold. First, it helps to highlight the main physical mechanisms behind the detachment of the APIs. In particular, we identified two modes of detachment, which we called, respectively, the northern hemisphere detachment mode and the southern hemisphere detachment mode. Secondly, the simplified model can be used as a sub-scale model in in Euler/Lagrange CFD simulations of inhalers. These approaches calculate the hydrodynamics and, by means of Lagrangian particle-tracking, the trajectories of the carrier particles in the inhaler.

Finally, our simplified model only accounts for one impact, while, in reality, the carrier will impact the inhaler's walls many times. However, as explained, the goal of this study is a detachment model implementable in CFD codes. During the CFD simulation, particle tracking will provide information on how many times (and with what velocity and angle) the carrier impacts the walls, while our model will provide information on the fraction of particles detaching at each impact. Similarly, our simplified model does not distinguish between API sticking to the wall and those free in the air and only the latter contribute to the dispersion efficiency of DPIs. However, CFD simulations can include a sticking efficiency parameter (e.g. [9,10,24]) that calculates how many particles colliding the wall will stick to it. In our case, the sticking efficiency can be included in our southern hemisphere detachment mode because only the APIs detaching from southern hemisphere will collide with the wall.

Coupling particle-tracking with the proposed simplified API detachment will allow new CFD models to also predict the actual number of APIs released and, therefore, the actual efficiency of dry powder inhalers.

Acknowledgements

This article is based upon work from COST Action (grant number: MP1404 SimInhale) "Simulation and pharmaceutical technologies for advanced patient-tailored inhaled medicines", supported by COST (European Cooperation in Science and Technology) (weblink: www.cost.eu).

Cost Description: COST (European Cooperation in Science and Technology) is a funding agency for research and innovation networks. Our Actions help connect research initiatives across Europe and enable scientists to grow their ideas by sharing them with their peers. This boosts their research, career and innovation.

The first author gratefully acknowledges the financial support received through a STSM (Short Term Scientific Mission) at the MPS laboratory, Institute of Process Engineering, Otto-von-Guericke University Magdeburg, D-06230 Halle (Saale), Germany.

References

[1] Z. Tong, W. Zhong, A. Yu, H.-K. Chan, R. Yang, CFD–DEM investigation of the effect of agglomerate–agglomerate collision on dry powder aerosolisation, J. Aerosol Sci. 92 (2016) 109–121.
[2] Z.B. Tong, H. Kamiya, A.B. Yu, H.K. Chan, R.Y. Yang, Multi-scale modelling of powder dispersion in a carrier-based inhalation system, Pharm. Res. 32 (2015) 2086–2096.
[3] G. Reychler, J.F. Dessanges, L. Vecellio, G. Reychler, J.F. Dessanges, L. Vecellio, Aérosols: Présent et futur, Rev. Mal. Respir. 24 (2007) 1013–1023.
[4] H.K. Chan, Dry powder aerosol delivery systems: current and future research directions, J. Aerosol Med. 19 (2006) 21–27.
[5] Q.T. Zhou, Z. Tong, P. Tang, M. Citterio, R. Yang, H.-K. Chan, Effect of device design on the aerosolization of a carrier-based dry powder inhaler—a case study on Aerolizer® Foradile®, AAPS J. 15 (2013) 511–522.
[6] W. Kaialy, A. Alhalaweh, S.P. Velaga, A. Nokhodchi, Influence of lactose carrier particle size on the aerosol performance of budesonide from a dry powder inhaler, Powder Technol. 227 (2012) 74–85.
[7] Y. Cui, S. Schmalfuss, S. Zellnitz, M. Sommerfeld, N. Urbanetz, Towards the optimisation and adaptation of dry powder inhalers, Int. J. Pharm. 470 (2014) 120–132.
[8] M. Sommerfeld, S. Schmalfuss, Numerical analysis of carrier particle motion in a dry powder inhaler, J. Fluids Eng. 138 (2016).
[9] J. Milenkovic, A.H. Alexopoulos, C. Kiparissides, Deposition and fine particle production during dynamic flow in a dry powder inhaler: a CFD approach, Int. J. Pharm. 461 (2014) 129–136.
[10] J. Milenkovic, A.H. Alexopoulos, C. Kiparissides, Flow and particle deposition in the turbuhaler: a CFD simulation, Int. J. Pharm. 448 (2013) 205–213.
[11] Y. Cui, M. Sommerfeld, Forces on micron-sized particles randomly distributed on the surface of larger particles and possibility of detachment, Int. J. Multiphase Flow 72 (2015) 39–52.
[12] Y. Cui, M. Sommerfeld, Application of lattice-Boltzmann method for analysing detachment of micron-sized particles from carrier particles in turbulent flows, Flow Turbul. Combust. 100 (2018) 271–297.
[13] Z.B. Tong, R.Y. Yang, A.B. Yu, S. Adi, H.K. Chan, Numerical modelling of the breakage of loose agglomerates of fine particles, Powder Technol. 196 (2009) 213–221.
[14] J.C. Yang, C.Y. Wu, M. Adams, DEM analysis of the effect of particle-wall impact on the dispersion performance in carrier-based dry powder inhalers, Int. J. Pharm. 487 (2015) 32–38.
[15] B. van Wachem, K. Thalberg, J. Remmelgas, I. Niklasson-Bjorn, Simulation of dry powder inhalers: combining micro-scale, meso-scale and macro-scale modeling, AICHE J. 63 (2017) 501–516.
[16] Y. Cui, M. Sommerfeld, The Detachment of Fine Drug Particles from Large Carrier Particles Via Wall Collisions within Dry Powder Inhalers, Part I: Particle-Wall Collision Model, Private Communication(To be submitted to Powder Technology) 2018.
[17] A. Alexiadis, The discrete multi-hybrid system for the simulation of solid-liquid flows, PLoS One 10 (2015).
[18] M. Ariane, S. Kassinos, S. Velaga, A. Alexiadis, Discrete multi-physics simulations of diffusive and convective mass transfer in boundary layers containing motile cilia in lungs, Comput. Biol. Med. 95 (2018) 34–42.
[19] H.P. Zhang, H.A. Makse, Jamming transition in emulsions and granular materials, Phys. Rev. E 72 (2005).
[20] N.V. Brilliantov, F. Spahn, J.M. Hertzsch, T. Poschel, Model for collisions in granular gases, Phys. Rev. E 53 (1996) 5382–5392.
[21] R.S. Bradley, The cohesive force between solid surfaces and the surface energy of solids, Philos. Mag. 13 (1932) 853–862.
[22] V.L. Popov, Contact Mechanics and Friction: Physical Principles and Applications, 2010.
[23] M. Sommerfeld, J. Kussin, Analysis of collision effects for turbulent gas-particle flow in a horizontal channel. Part II. Integral properties and validation, Int. J. Multiphase Flow 29 (2003) 701–718.
[24] J. Milenkovic, A.H. Alexopoulos, C. Kiparissides, Optimization of a DPI inhaler: a computational approach, J. Pharm. Sci. 106 (2017) 850–858.